Review of Scientific Instruments ARTICLE pubs.aip.org/aip/rsi

Improving the quality of x-ray mirrors: An inter-lab, optical metrology collaboration to guide deterministic polishing

Cite as: Rev. Sci. Instrum. 96, 081305 (2025); doi: 10.1063/5.0287341
Submitted: 24 June 2025 • Accepted: 31 July 2025 •
Published Online: 27 August 2025

Simon G. Alcock,[1,a] Ioana-Theodora Nistea,[1] Murilo Bazan da Silva,[1] Kawal Sawhney,[1] Norman Niewrzella,[2] Holger Lasser,[2] Amparo Vivo,[3] Ray Barrett,[3] Jana Buchheim,[4] Grzegorz Gwalt,[4] Frank Siewert,[4] Sibylle Spielmann,[5] Uwe Flechsig,[5] Silja Schmidtchen,[6] Maurizio Vannoni,[6] Josep Nicolas,[7] Muriel Thomasset,[8,9] and Francois Polack[8]

AFFILIATIONS

[1] Diamond Light Source Ltd, Harwell Science and Innovation Campus, Didcot OX11 0DE, United Kingdom
[2] ZEISS, SMT GmbH, Carl-Zeiss-Str. 22, 73447 Oberkochen, German
[3] ESRF, The European Synchrotron, 71 Avenue des Martyrs, 38043 Grenoble, France
[4] Helmholtz Zentrum Berlin, Albert-Einstein-Strasse 15, 12489 Berlin, Germany
[5] Paul Scherrer Institut, PSI, 5232 Villigen, Switzerland
[6] European X-Ray Free-Electron Laser Facility, Holzkoppel 4, 22869 Schenefeld, Germany
[7] ALBA Synchrotron Light Source, Carrer de la Llum 2-26, Cerdanyola del Vallès 08290, Spain
[8] Synchrotron SOLEIL, L'Orme des Merisiers, Départementale 128, 91190 Saint Aubin, France
[9] Centre de Nanosciences et de Nanotechnologies, CNRS, Université Paris-Saclay, Palaiseau, France

Note: This paper is part of the Special Topic on the 8th International Workshop on X-Ray Optics and Metrology.
[a] **Author to whom correspondence should be addressed:** simon.alcock@diamond.ac.uk

ABSTRACT

The surface quality of x-ray mirrors is a major constraint on optical performance at synchrotron light and free electron laser facilities. A limiting factor for creating state-of-the-art optics is the accuracy of metrology data to deterministically guide the polishing tool to correct surface errors. The "MooNpics" (Metrology On One-Nanometer-Precise Optics) collaboration aims to improve optical metrology capabilities at European facilities to enable reproducible measurement of long or curved optics with height errors <1 nm rms and slope errors <100 nrad rms. Three challenging x-ray optics were measured by several labs using a variety of instruments. The mirrors, chosen to challenge and explore different aspects of optical metrology, were as follows: a 1 m-long, ultra-flat (radius of curvature R > 100 km); an ellipse with added parabolic arcs; and a strongly curved sphere (R ~ 9.3 m) with an added spatially varying chirp. This study highlighted calibration issues with several instruments, which were subsequently corrected. In this paper, we present results about the ellipse mirror. Based on metrology data provided by the collaboration, two cycles of ion beam figuring improved all aspects of the mirror, including correcting the ellipse parameters, reducing high- and mid-frequency spatial polishing errors, and refining the shape of the parabolic arcs. Overall, the slope and height errors were improved by a factor of ~10. We also show how the round-robin measurement exercise helped refine "best practice" procedures for mounting optics, alignment, and data acquisition and analysis methods. It is hoped that this collaborative project will ignite further improvements in the production quality of x-ray optics to benefit many scientific communities around the world.

I. INTRODUCTION

Optical quality of x-ray mirrors and grating substrates[1–3] limits the performance of many beamlines at synchrotron light (SL) and free electron laser facilities (XFEL). State-of-the-art x-ray optics with height errors <1 nm rms are typically finished using deterministic polishing techniques, such as ion beam figuring (IBF),[4–7] fluid jet polishing (FJP),[8] elastic emission machining (EEM),[9,10] differential deposition (DD),[11–13] or magnetorheological finishing (MRF).[14–16] A significant challenge for deterministic polishing is acquiring accurate metrology data to guide the polishing tool to correct residual errors on the optical surface.

There are currently only a few suppliers around the world who can produce the highest-grade optics required by third and fourth generation accelerator-based light sources. In recent years, for economic reasons, several companies no longer produce such optics, instead concentrating on high-budget projects for EUV lithography, military, space, and astronomy applications. To mitigate the supply-chain risk for procuring x-ray optics, many SL and XFEL facilities are now developing in-house fabrication infrastructure and capabilities, including polishing and coating technologies.

In synergy with this approach, it is important to support commercial suppliers to improve their metrology and polishing capabilities. The "MooNpics" project (Metrology On One-Nanometer-Precise Optics),[17] funded as part of "HORIZON 2020" CALIPSO-plus, is a collaboration between several European manufacturers of x-ray mirrors and optical metrology labs at SL and XFEL labs. The goal of the project is to enable the production of enhanced quality x-ray mirrors, by improving metrology reproducibility and accuracy. One of the main tasks of the MooNpics project was a "Round-Robin" measurement exercise, whereby three, challenging x-ray optics were characterized at various facilities using a range of different metrology instruments. The shared optics were as follows: a 1 m-long, ultra-flat mirror, an elliptical mirror with added parabolic arcs, and a strongly curved sphere (radius of curvature R ~ 9.3 m) with an added spatially varying chirp. Each optic was chosen to challenge and explore different aspects of metrology. Such instruments, which are broadly representative of usage within the optics testing community, include slope profilometers, such as the nanometer optical measurement (NOM) systems and long trace profilers (LTP);[18–24] sub-aperture stitching Fizeau- and micro-interferometers;[25–34] wavefront sensors; and x-ray "at-wavelength" techniques.[35–38] To put this challenge into context, accuracy is required over a dynamic range greater than 1×10^6 (i.e., ratio between resolving angle changes of a few nanoradians over a measurement range of several milliradians). Unfortunately, many factors reduce the accuracy of optical metrology and compromise the final production quality of x-ray mirrors. Such errors include systematic instrumental errors; fluctuations in air temperature, pressure, and humidity; mechanical strain induced by the opto-mechanical holder; gravity sag caused by positional errors of the support points; and numerical errors during data analysis, such as artifacts from sub-aperture stitching. All such errors need to be carefully controlled to improve overall accuracy. Studying the same optics using different instruments also provides valuable information about the limitations and strengths of each metrology device.

In this paper, we describe a study of a three-lane elliptical mirror with parabolic arc surface modifications. To ensure repeatability of alignment and test conditions at the participating facilities, a series of fiducial marks were added to the mirror. This proved to be highly beneficial for precise alignment of measurement and analysis regions. As an extension to the project, and a clear demonstration of how accurate metrology can aid the production of improved quality x-ray mirrors, two cycles of ion beam figuring were shown to improve all aspects of the optical profile.

II. EXPERIMENTAL

A. Round-robin

Round-robin measurement exercises[39–41] have previously provided valuable information about x-ray optics and metrology instruments, including standardization of measurement and analysis techniques. Commercial partners involved in the MooNpics project were WinlightX (now Bertin-Winlight) (France) and ZEISS (Germany). SL and XFEL labs represented were Diamond Light Source (UK), ALBA (Spain), ESRF (France), European-XFEL (Germany), HZB (Germany), PSI (Switzerland), and Soleil (France). The round-robin was coordinated by the European-XFEL. Three phases of measurements were conducted on the elliptical mirror before ion beam figuring (initial state), after first cycle of ion beam figuring "IBF1" (intermediate), and after second cycle of IBF "IBF2" (final state). Table I summarizes which instruments measured the mirror throughout the process.

B. Optical specification

The three-lane ellipse mirror is the result of a previous R & D project to create expanded x-ray beams with a homogeneous cross-sectional profile.[42] The mirror, as described in Table II, was originally manufactured in 2015 by ZEISS with three "lanes," each polished to the same elliptical profile (radius of curvature ~264 m at the center of the mirror). Lane 1 is a pure ellipse, while lanes 2 and 3 have additional parabolic arc height modulations to expand the x-ray beam. Figure 1 shows Fizeau interferometry of the optical surface (after removal of best-fit ellipse), demonstrating the two periods of parabolic arcs on Lanes 2 and 3.

C. Opto-mechanical support

Gravitational sag can play a significant role on the nanometer scale for vertically focusing optics.[43] To mitigate this issue, for instruments measuring the optic with its surface normal facing

TABLE I. Summary of optical measurements of the x-ray mirror.

Facility and instrument	Before IBF	After first cycle of IBF (IBF1)	After second cycle of IBF (IBF2)
ALBA-NOM	✓		
Diamond-HDX		✓	✓
Diamond-NOM	✓	✓	✓
ESRF-LTP	✓	✓	
HZB-NOM	✓		✓
PSI-LTP	✓		
Soleil-LTP		✓	
WinlightX-Fizeau	✓		
XFEL-Fizeau		✓	

TABLE II. Specifications of the elliptical x-ray mirror.

Parameter	Value
Material	Single-crystal Si(100)
Coating	None
Dimensions	160 (L) × 90 (W) × 50 (H) mm
Active length/clear aperture	100 mm
Distance from source to center of the mirror, p	46 m
Distance from the center of the mirror to focus, q	0.40 m
Angle of incidence at the center of the mirror, θ	3 mRad
Peak-to-valley of two periods of parabolic arcs added to ellipse profile	Lane 1 = 0 (pure ellipse) Lane 2 = 25 nm Lane 3 = 50 nm

upward, the optic was supported on 3× stainless steel balls positioned at the Bessel points (separated by 0.559 times the length or width of the mirror). For consistency, the support balls were shipped with the mirror to each facility. For sideways-facing measurements, the optic was supported on a flat plate or soft cloth (e.g., TEXWIPE) to minimize point-load Poisson distortions or anticlastic bending.[44] Typically, x-ray mirrors are mounted and measured in their beamline opto-mechanical holders. Soft clothes are only used on the rare occasion when opto-mechanics cannot be dismounted from the vacuum vessel/motion systems.

D. Fiducial markers

Deterministic polishing relies on carefully positioning the correction tool relative to surface errors. A general rule recommends in-plane positional accuracy better than 10% of the diameter of the polishing tool. Various technologies are used to determine the location of the polishing tool relative to the substrate, including vision systems with a zoom lens and CCD camera; on-board metrology instruments;[45] mechanically contacting the mirror against hard-stops, which have been surveyed into position using a coordinate measuring machine (CMM); direct imaging of the ion beam's location using *in situ* diagnostics such as a Faraday cup; and post-processing using an external metrology device.

In preparation for the MooNpics project, several sets of fiducial markers were added outside the clear aperture of the mirror by ZEISS to aid dimensional alignment. Figure 2 illustrates these features, which include inscribed lines on the end faces of the substrate to indicate the location of each lane; laser-etched cross-hairs; and strategically positioned dots and lines created using ion beam figuring. In synergy, the markers provide a fixed coordinate system to uniquely locate features on the optical surface to a precision better than 100 μm. This enables accurate alignment of the mirror relative to each metrology instrument, thereby improving reproducibility of measurement and selection of surface data for comparative analysis. The various fiducial markers were chosen to be visible to different types of metrology instruments. For example, the cross-hairs provide visible feedback for positioning the optic relative to the encoded translation scan stages of stitching micro-interferometers and to aid careful extraction of 1D analysis lines from 2D Fizeau interferometry scans. Correspondingly, the ion beam dots (depth ~200 nm, width ~2.3 mm FWHM) and ion beam lines (depth ~50 nm, width ~2 mm) help align instruments that only record 1D line scans, such as slope profilometers.

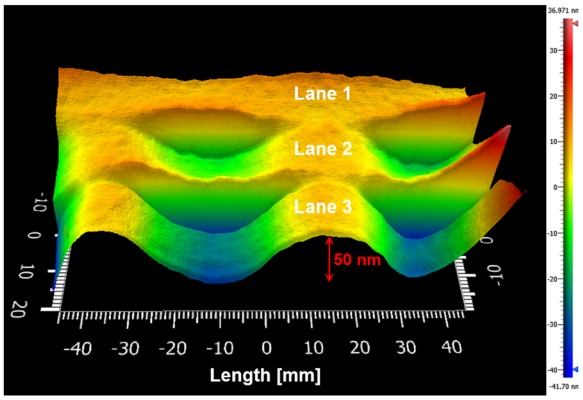

FIG. 1. Fizeau interferometry of the mirror showing the surface errors and height modulations of the three lanes (after removal of the ellipse profile). Lane 1 is a pure ellipse, whereas lanes 2 and 3 have added parabolic arcs to create expanded x-ray beams with a homogeneous cross section.

E. Data analysis

To achieve experimental reproducibility,[30,31] the same region of interest must be measured and analyzed by all. This is imperative for aspheric surfaces, such as an ellipse, since variations in selection will influence the best-fit parameters. The center of the analysis region was defined to be equidistant between the pairs of fiducial lines and dots, which are at nominal distances of ±60 and ±70 mm from the center of the optic, respectively. Calculating the spatial derivative of the slope profile, d^2z/dx^2, provides a more precise method to locate fiducial features to define the central 100 mm "clear aperture" analysis region of the mirror. The fixed distance between the pairs of fiducial features also helps calibrate instrument magnification factors. For example, a lateral scaling factor was applied to stretch the data to correct small discrepancies in the zoom factor of Fizeau- or micro-interferometers to <0.1%. The upper and lower rows in Fig. 3 show the second derivative of height for three instruments

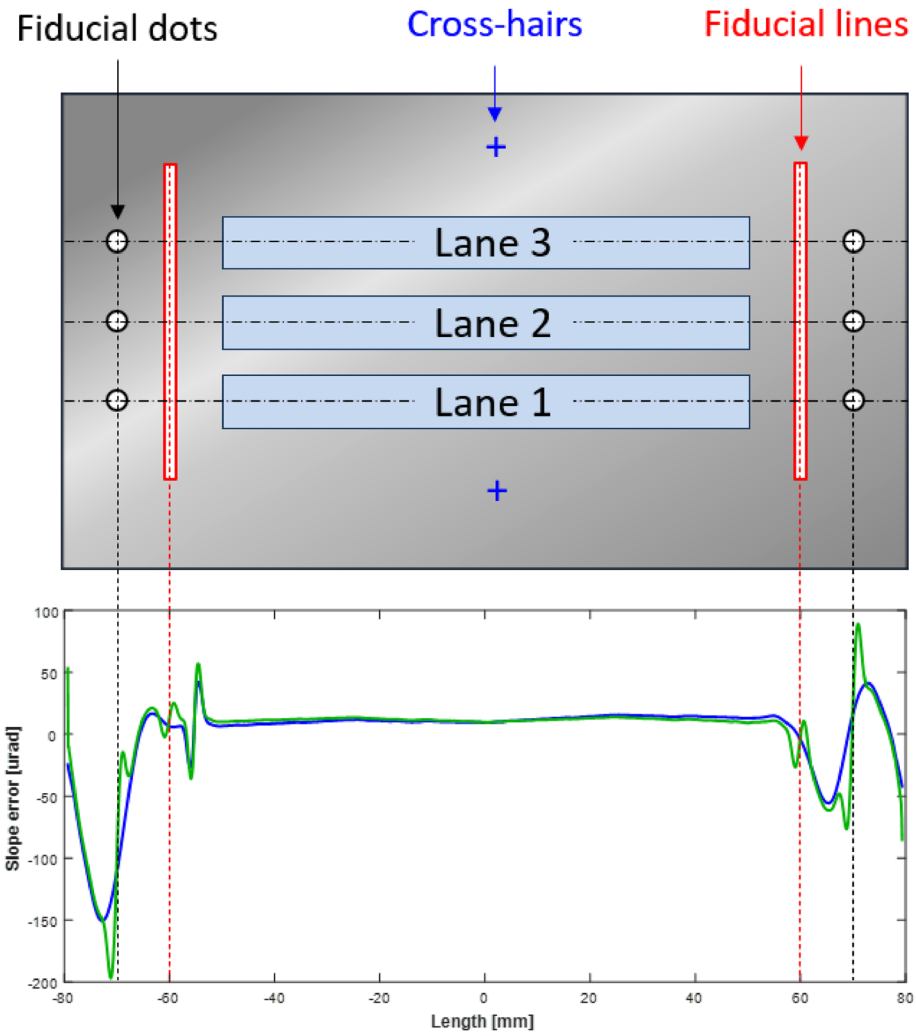

FIG. 2. Series of fiducial markers were inscribed on the optical surface to reproducibly locate the polishing errors and guide the correction tool. The upper image shows a plane view of the optical surface, including: the three lanes, cross-hairs, and fiducial lines and dots added by ion beam figuring. The lower plot shows a 1D slope error scan along the pure ellipse Lane 1 before (blue curve) and after (green curve) the fiducials were added.

before and after small translations (typically a few tens of micrometers), respectively, and scaling corrections were applied to align all datasets. For this study, the spatial sampling of the Diamond-NOM, HDX Fizeau, and Bruker GTX micro-interferometer were 100, ~45, and 7 μm, respectively. The location of the residual polishing defects on the optical surface also provides a convenient verification of the positioning and stretching of datasets.

For consistency, all datasets were analyzed using Diamond's standard ellipse-fitting algorithms, based on the exact expressions for the height z or slope dz/dx profile of an ellipse, as derived by Sutter,[46]

$$z\ (x,\ p,\ q,\ \theta) = \frac{(p+q)\sin\theta}{(p+q)^2 - (p-q)^2\sin^2\theta} \times \left[2pq + [(p-q)\cos\theta] \times x \pm 2\sqrt{pq}\sqrt{pq + [(p-q)\cos\theta]x - x^2}\right] \quad (1)$$

$$\frac{dz(\boldsymbol{x},\ \boldsymbol{p},\ \boldsymbol{q},\ \boldsymbol{\theta})}{dx} = \left(\frac{(p+q)\sin\theta}{(p+q)^2 - (p-q)^2\sin^2\theta}\right) \times \left[(p-q)\cos\theta - \sqrt{pq}\left(\frac{(p-q)\cos\theta - 2x}{\sqrt{pq + [(p-q)\cos\theta]x - x^2}}\right)\right]. \quad (2)$$

The best-fit ellipse was calculated, using a generalized reduced gradient (GRG) nonlinear algorithm, by varying θ about its specified value to minimize the rms slope error. Other fittings were also considered by varying θ and/or q to minimize height error rms. Prior experience using synthetic datasets to model the height or slope errors (e.g., high-order polynomials or Fourier series, with exact expressions for integral or differential versions) showed that calculation errors from numerical integration or differentiation could be kept to negligible levels if data acquired by height-measuring

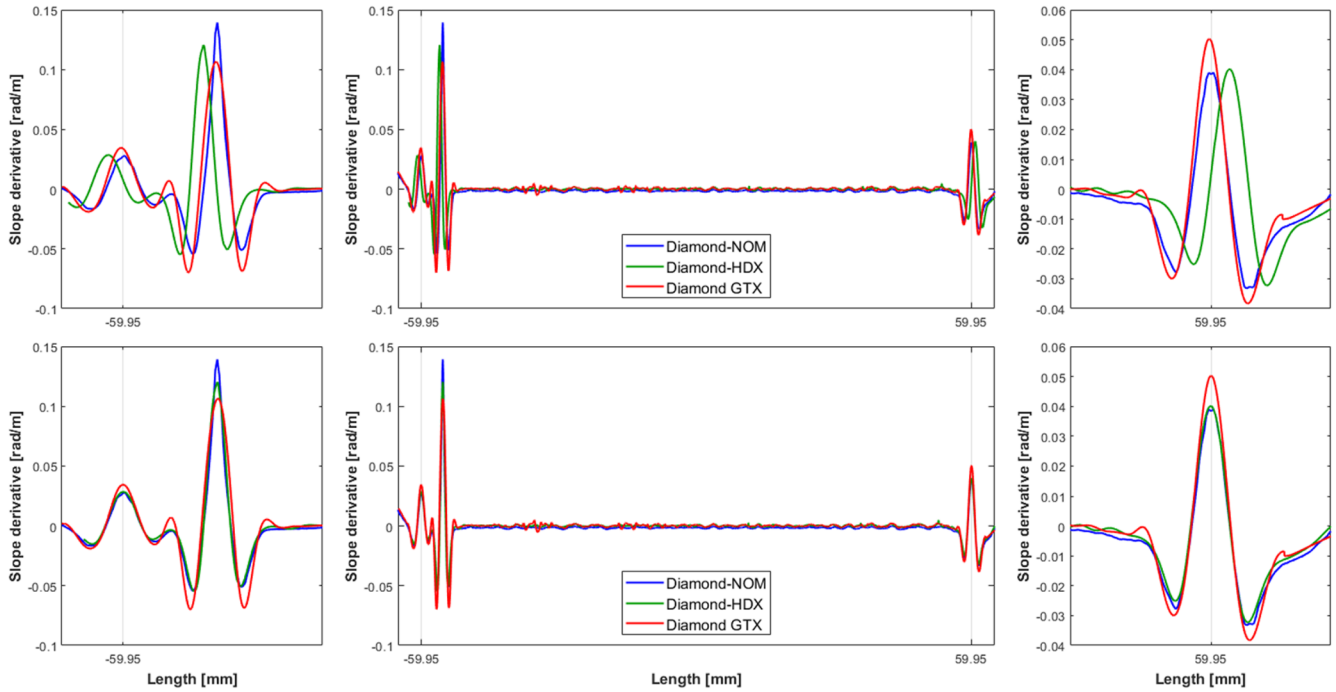

FIG. 3. Calculating the second differential of height d^2y/dx^2 enables the centers of the fiducial dots and lines to be more precisely determined, thus enabling better comparison between different datasets. Upper row: before alignment of datasets from three different metrology instruments, showing small variations in stretching and positioning. Lower row: after alignment and correction, showing perfect coincidence to <50 μm. The outer columns show a zoomed region around the fiducial markers at each end of the mirror.

instruments (such as Fizeau interferometers) are fitted using the height-version of the exact form of the ellipse [Eq. (1)], and data from slope-measuring instruments (such as a NOM) are fitted using the slope equation for the ellipse [Eq. (2)]. Numerical integration or differentiation of slope errors and height errors were then performed using standard in-built algorithms in MATLAB and python. Characterizing the same optic using the various instruments, and computing the power spectral density (PSD) of height errors, provides important information about the spatial sensitivity of each device, including the point spread function and instrument transfer function.[47–49] This approach guides the choice of Fourier filtering parameters. After removal of the best-fit or specified ellipse from the height data acquired by the two interferometers, a low-pass filter of 2 mm was applied prior to numerical differentiation to match to the in-plane resolution of the autocollimator of the Diamond-NOM. Conversely, the unfiltered Diamond-NOM slope error profile was numerical integrated for comparison with the unfiltered height error data from the interferometers.

III. RESULTS

A. Phase-I: Before ion beam figuring

Figure 4 shows the slope error of lane 1 (pure ellipse) of the mirror, as measured by the various instruments at different optical metrology labs. The left plot shows an "absolute" comparison by removing the same specified ellipse parameters (as listed in Table II) from all datasets. The right plot shows a "relative" comparison by removing a unique best-fit ellipse from each dataset by varying the angle of incidence θ to minimize the rms slope error.

Figure 5 shows the corresponding "absolute" slope errors for lanes 2 (left plot) and 3 (right plot). The parabolic arcs in height correspond to piecewise-triangular profiles in slope, with peak-to-valley (PV) of ~5 and 10 μrad for lanes 2 and 3, respectively. The inclination of the slope error curves after removal of the specified ellipse reveals the mirror consistently has an error of ~1% in its curvature across all three lanes (PV deviation of a few microradians compared to the mirror's slope range of ~382 μrad).

Table III shows that the best-fit angle θ (compared to the specified value of 3 mrad) was within ±0.16% of the average for all but one instrument. The outlier had a difference in θ of ~2.4% compared to the average of the other instruments. This round-robin comparison successfully identified an offset bias with the curvature of a Fizeau interferometer's transmission flat, which was subsequently corrected, thereby improving measurement reproducibility. The variation in the slope error rms values after removal of the best-fit ellipse is dominated by low-spatial frequency errors (e.g., rms for lane 1 varies between 1084 and 1640 nrad). However, as expected, improved agreement was observed between all instruments after removal of the individual best-fit ellipse for each dataset, leading to tighter clustering of the rms values (e.g., rms for Lane 1 varies between 454 and 593 nrad). A further point of note is the differences in high-spatial frequency content measured by each instrument, which is inherent to the probe/pixel size and the ITF.

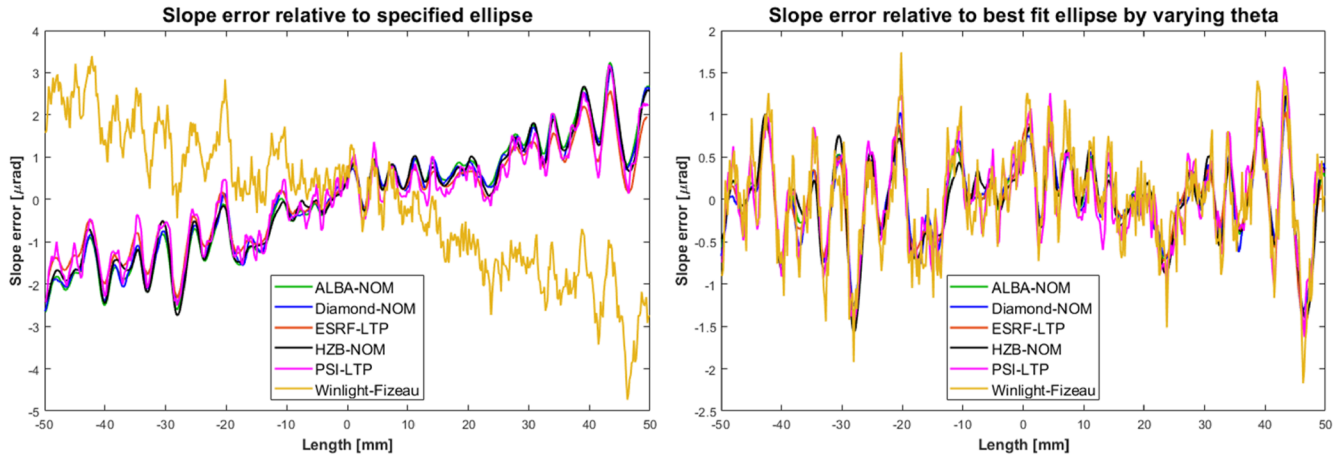

FIG. 4. Slope error of lane 1 of the mirror, before ion beam figuring and after removal of the specified ellipse (left plot) or best-fit ellipse by varying the angle of incidence θ (right plot).

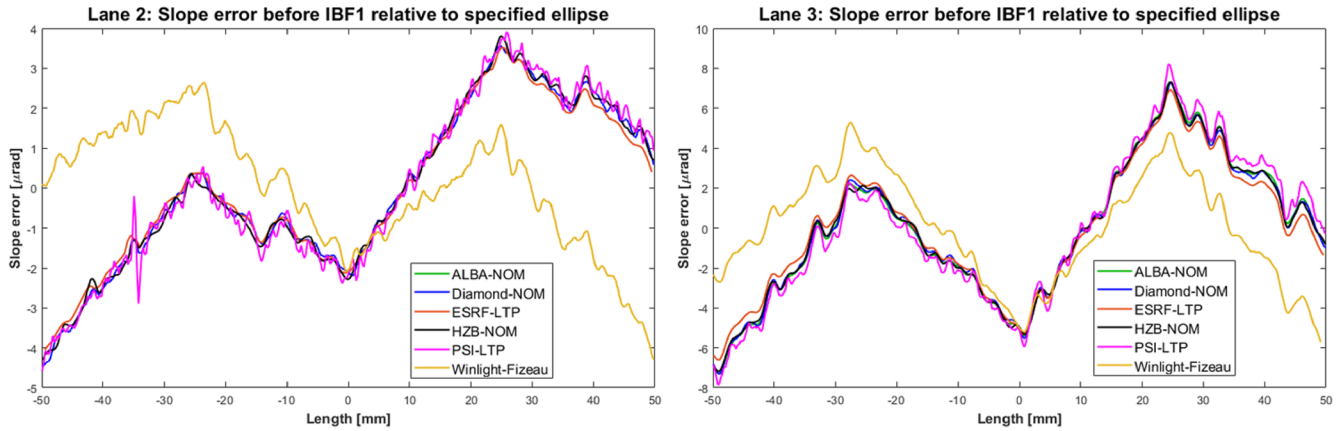

FIG. 5. Slope error of lane 2 (left plot) and lane 3 (right plot) of the mirror, before IBF, relative to specified ellipse.

TABLE III. Slope error of the three lanes of the mirror, as measured by each instrument, after removal of the specified ellipse and parabolic arc modifications (absolute metrology) or best-fit ellipse (relative metrology).

	Slope error rms (S.E) and best fit value of ellipse parameter θ								
	Lane 1			Lane 2			Lane 3		
	Specified ellipse	Best fit ellipse		Specified ellipse	Best fit ellipse		Specified ellipse	Best fit ellipse	
Instrument	S.E (nrad)	S.E (nrad)	θ (mrad)	S.E (nrad)	S.E (nrad)	θ (mrad)	S.E (nrad)	S.E (nrad)	θ (mrad)
ALBA-NOM	1376	454	3.0353	1804	266	3.0485	2244	624	3.0586
Diamond-NOM	1302	456	3.0332	1713	246	3.0462	2159	601	3.0565
ESRF-LTP	1084	464	3.0265	1580	256	3.0422	1854	616	3.0462
HZB-NOM	1308	491	3.0330	1736	284	3.0466	2179	620	3.0568
PSI-LTP	1174	545	3.0283	1814	379	3.0478	2589	752	3.0673
WinlightX-Fizeau	1640	593	2.9585	1098	336	2.9716	912	606	2.9814

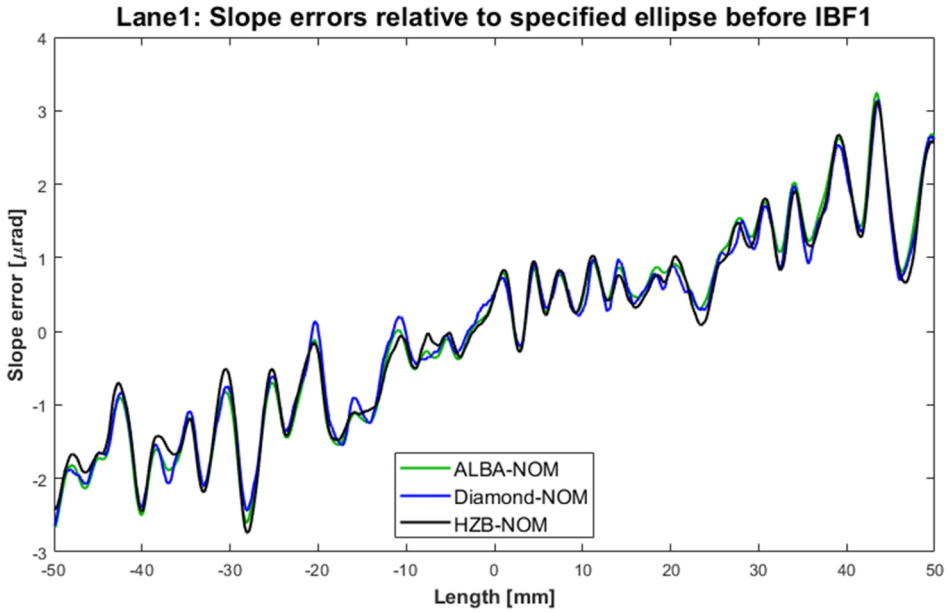

FIG. 6. After removal of identical ellipses from all datasets, exceptional reproducibility was obtained in the "absolute" slope error of the mirror as measured by the three "NOM" slope profiler instruments at Diamond, ALBA, and HZB. Representative data from Lane 1 are shown for brevity, with similar levels of agreement observed for lanes 2 and 3. An average of these datasets was sent to guide the first IBF deterministic correction at ZEISS.

Figure 6 demonstrates the exceptional reproducibility in the absolute measurements made by the three NOM instruments (which employ the same model of Elcomat3000 autocollimator from Möller-Wedel Optical, Germany), both in terms of the measured ellipse parameters and the spatial sensitivity of residual polishing errors of the mirror. The best-fit ellipse parameter θ for each lane varied by <0.01% as recorded by the Diamond-NOM and HZB-NOM. Comparable results were achieved for lanes 2 and 3. 1D-line profiles were averaged across ~3.5 mm of the width of the optic due to the diameter of the aperture defining the size of the autocollimator beam. The average of the three NOM datasets for each of the three lanes was provided as the input for the first IBF deterministic correction at ZEISS using their proprietary, height-based, dwell-time algorithms. Repolishing aimed to improve the low-spatial frequency errors (ellipse), mid-spatial frequency (parabolic arc shapes), and high-spatial frequency (polishing errors) of the mirror. NOM data were chosen to guide the IBF correction, rather than higher resolution topography acquired by Fizeau- or micro-interferometers. This is because the ITF of the NOM,[50,51] which starts to diminish in sensitivity for spatial periods <2 mm, is similar in dimension to the finest ion beam used at ZEISS.

B. Phase-II: After first cycle of ion beam figuring

After the first iteration of ion beam figuring at ZEISS, Fig. 7 shows the slope error of lane 1 (pure ellipse) of the mirror, as measured by the Diamond-NOM, Diamond-HDX Fizeau,[30] ESRF-LTP,

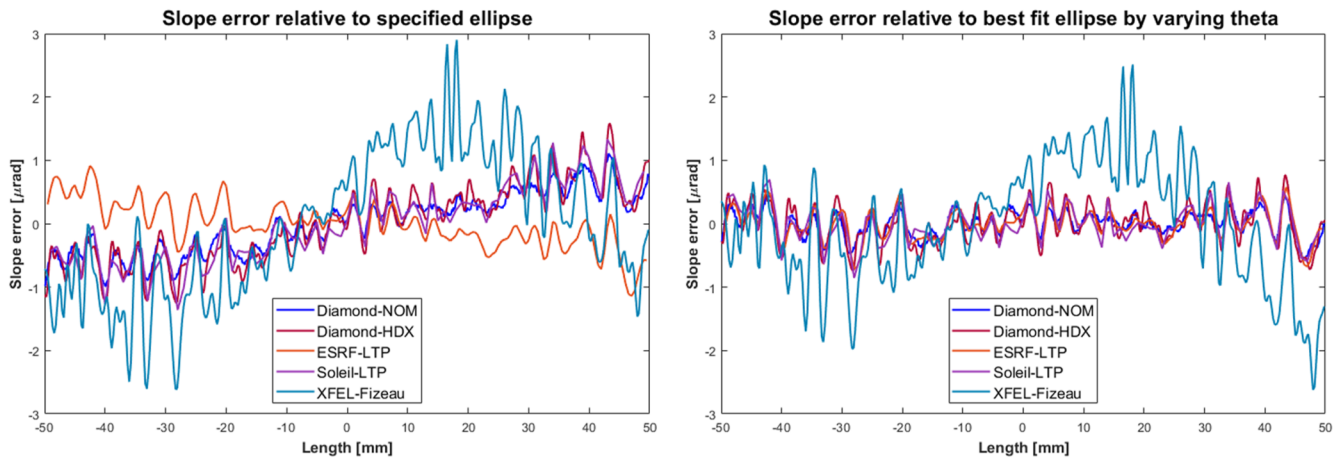

FIG. 7. Slope error of lane 1 after the first cycle of ion beam figuring, relative to the specified ellipse (left plot) and relative to the best-fit ellipse (right plot).

TABLE IV. Slope errors and best-fit ellipse parameters for each lane of the mirror after the first cycle of ion beam figuring.

	Slope error rms (S.E) and best fit value of ellipse parameter θ								
	Lane 1			Lane 2			Lane 3		
	Specified ellipse	Best fit ellipse		Specified ellipse	Best fit ellipse		Specified ellipse	Best fit ellipse	
Instrument	S.E (nrad)	S.E (nrad)	θ (mrad)	S.E (nrad)	S.E (nrad)	θ (mrad)	S.E (nrad)	S.E (nrad)	θ (mrad)
Diamond-NOM	470	197	3.0117	615	168	3.0161	875	334	3.0220
Diamond-HDX	597	294	3.0142	664	233	3.0169	952	402	3.0235
ESRF-LTP	364	242	2.9926	...	...	...	...	...	...
Soleil-LTP	598	308	3.0143	729	232	3.0187	923	394	3.0224
XFEL-Fizeau	1136	922	3.0179	1336	846	3.0280	1360	850	3.0286

Soleil-LTP, and Eu-XFEL-Fizeau. The left plot shows the absolute slope error residual after removing the specified ellipse, and the right plot shows the relative slope error after removal of a best-fit ellipse by varying the angle of incidence θ. The comparisons are also representative of measurements of lanes 2 and 3, as demonstrated in Table IV.

Table IV and Fig. 7 show that the curvature of the mirror was improved (θ closer to 3 mrad: average value after IBF was 3.0195 mrad, compared to 3.0449 mrad), as were the shape of the parabolic arcs and the polishing marks (slope error rms value reduced for best-fit ellipse). The best fit value for θ varied by <0.25% and was <0.01% for several instruments, which is significantly better than the typical procurement acceptance tolerance of <0.5% error in the mirror's curvature. However, despite the overall form improvement, the correction did not fully correct the slope errors. To investigate why, the left image shown in Fig. 8 compares what was requested to be removed vs what was actually removed for each of the three lanes (i.e., difference between measurements of mirror before and after IBF correction). There is correlation between the pairs of datasets, but the ratio between the removal and the requested profiles is consistently ~0.7 for all three lanes. If this vertical scaling factor is applied, the right image in Fig. 8 shows a strong correlation between the requested removal and the actual removal profiles. This suggests that the ion beam removal rate was 30% less than requested, perhaps due to a prior miscalibration, or a gradual reduction in effectiveness during the lifetime of components.

Aside from amplitude scaling issues, there are two further sources of error that can limit the final quality of the mirror, namely, lateral shifts and lateral scaling errors between the measured surface topography and the deterministic correction tool's motion trajectory. A simple numerical model was developed to investigate how such issues contribute to non-ideal convergence of surface material removal. This approach assumes idealized measurements, with negligible random errors, and constant systematic errors. Two identical versions of synthetic data were generated by interpolating experimental measurements of the mirror's slope error profile $S(x)$ to a

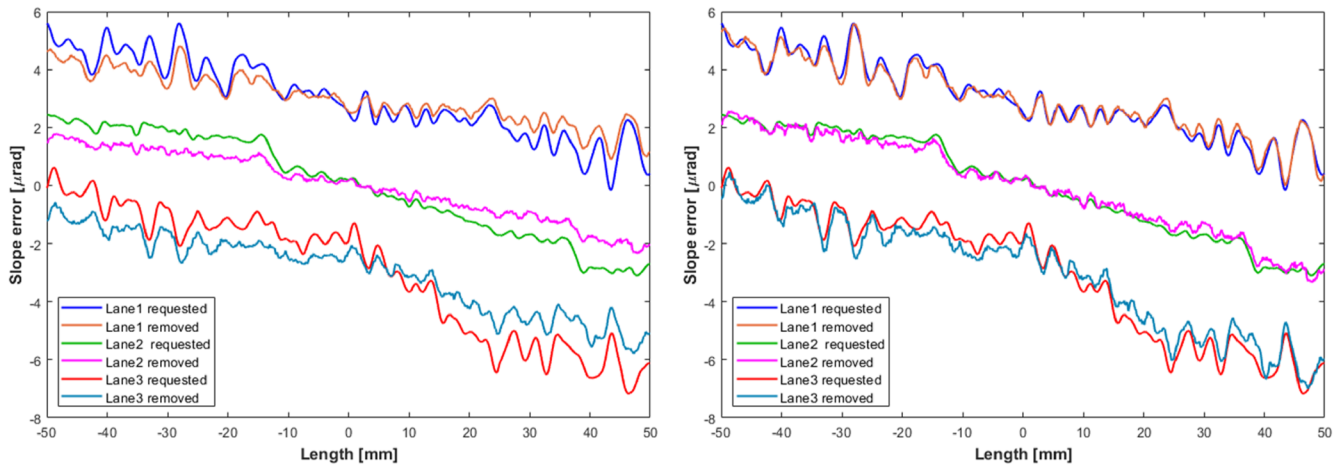

FIG. 8. Left image shows the requested slope error corrections for the first cycle of IBF for each lane of the mirror, compared to what was measured to be physically removed. Curves are offset vertically for clarity. After vertically scaling by ~0.7, excellent agreement is obtained between the datasets, indicating a miscalibration in the ion beam removal function.

finer grid of points (to enable discrete data points to be matched). Modifications were made to one copy by applying amplitude scaling a, lateral scaling b, and shift c along the length of the mirror (x axis) to mimic errors with deterministic polishing. The difference $D(x)$ between the unmodified and modified synthetic slope error profiles corresponds to the residual errors expected after non-ideal polishing,

$$D\ (x) = S(x) - a \times S(bx + c). \tag{3}$$

For an optical surface with random topography, the magnitude of amplitude scaling a will dominate the rms value of the difference profile $D(x)$, with reduced influence from lateral scaling b and shift c of the x-axis. However, x-ray mirror surfaces often have pseudo-periodic "texture" generated by the polishing process. For textured surfaces, non-unity values for the parameter b can lead to interference "beats" in the residual error D. While if c is close to a half-integer value of the surface texture period, constructive interference of the two profiles will occur, leading to an increase in the rms value. In general, the stronger the surface periodicity, the greater the contribution to D from errors from scaling b and shift c of the x axis.

Analysis of data in Fig. 8, using the basic model described above, calculates $a \sim 0.7$, $b \sim 0$, and $c \sim 0$. This indicates that the removal rate was 0.7 times the demanded value, and that the ion beam was well-aligned with surface defects on the mirror. However, on several past occasions, "beat" frequencies were observed in the slope error profile of deterministically polished optics from different manufacturers. This is indicative of small miscalibration of the lateral scaling factor and translation offsets, either caused by an incorrect zoom factor of the metrology instrument, or systematic errors in the translation stages of the polishing system. To quantify their influence, the parameters a, b, and c were incrementally varied, and the rms of D was calculated for each case. To achieve a slope error $D < 100$ nrad rms, the following criteria needed to be met: $0.95 < a < 1.05$; $0.998 < b < 1.002$; and $|c| < 0.1$ mm. These values are derived from the polishing marks on this specific mirror, but it is hoped that such analysis provides general order-of-magnitude estimates for correction of high-quality mirrors. If two or more correction errors are present, the above-mentioned tolerances become stricter. Figure 9 shows examples of the additional slope errors introduced for non-ideal: lateral scaling factor, b, and lateral shift errors, c (left plot); or removal rate, a, and lateral shift errors, c (right plot).

C. Phase-III: After second cycle of IBF

After the second iteration of ion beam figuring at ZEISS, the mirror was remeasured at Diamond and HZB. Figure 10 shows the Diamond-NOM, Diamond-HDX Fizeau, and HZB-NOM measurements of the slope error (left image) and height error (right image) for lane 1, relative to the best-fit ellipse. Table V lists the rms values for slope error and the best-fit ellipse parameter θ.

Figure 11 shows the comparison between what was requested to be removed vs what was physically removed for each of the three lanes. Only very small adjustments were required for the fit parameters a, b, and c. This demonstrates that the IBF removal rate and location were very close to the target values, both for low- and high-spatial frequency surface errors.

D. Summary of improvements

Based on accurate metrology data provided by the project consortium, two cycles of ion beam figuring improved the height error and slope error of all three lanes of the optic by a factor of ~10. Plots in the left column of Fig. 12 show the slope error for each of the 3

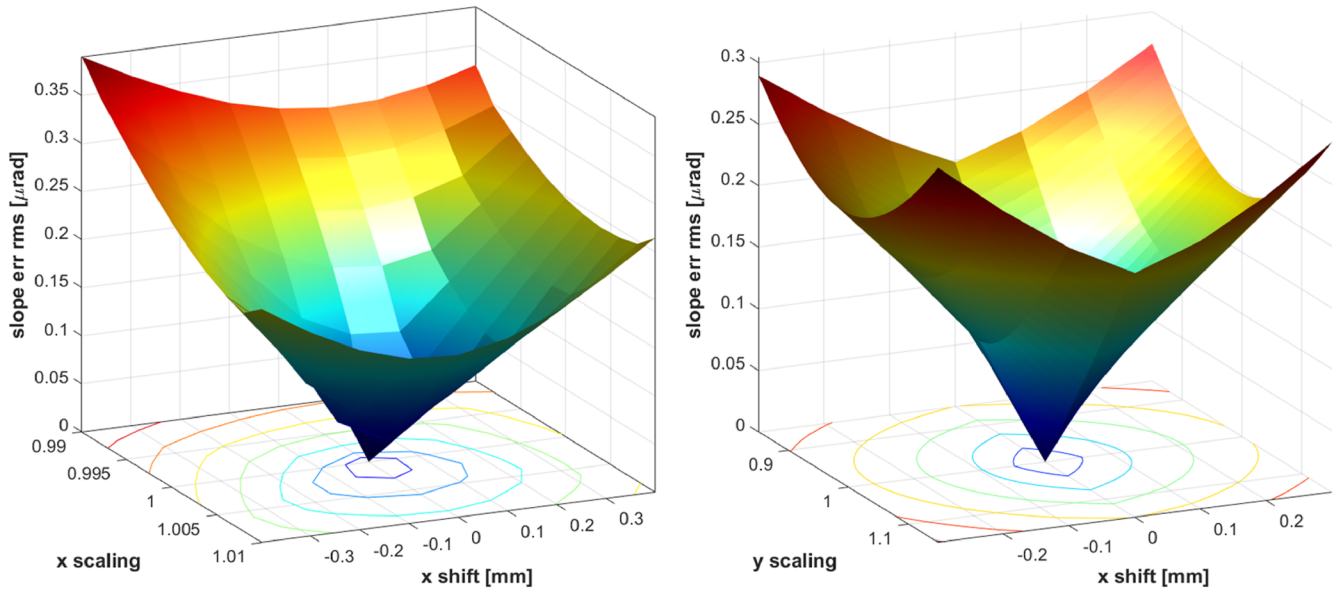

FIG. 9. Vertical axis shows the rms value of the simulated slope error when varying the lateral scaling b and lateral shift c (left image), or the vertical scaling a and lateral shift c (right image). Such plots can be used to predict likely tolerances required for deterministic correction to achieve a given level of slope errors.

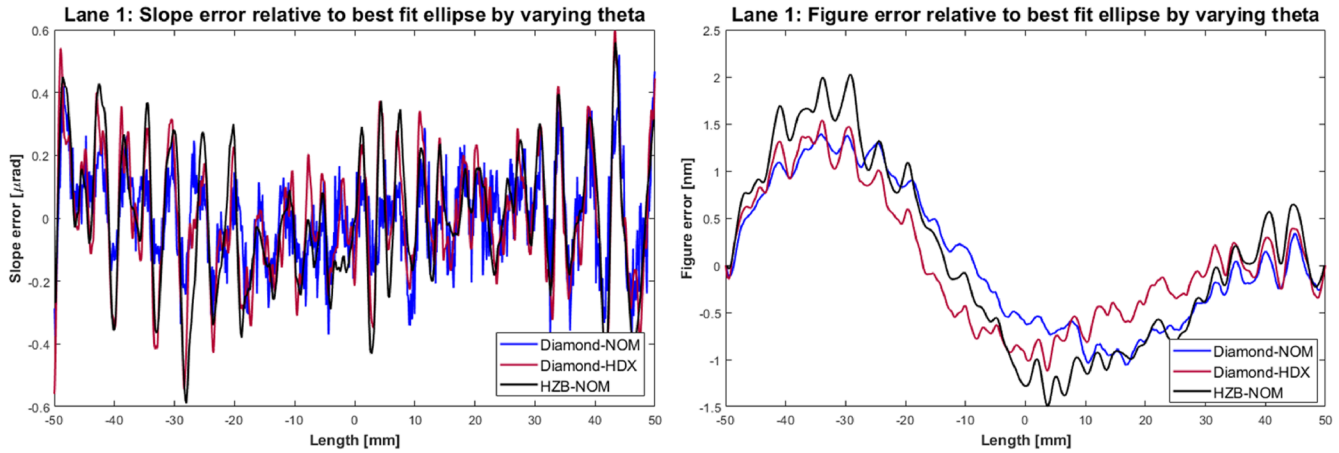

FIG. 10. Slope error (left image) and height error (right image) for lane 1 of the mirror after the second cycle of ion beam figuring, relative to the best fit ellipse and parabolic arcs, as measured by the Diamond-NOM, Diamond-HDX Fizeau, and the HZB NOM.

TABLE V. Slope errors and best-fit ellipse parameters for each lane of the mirror after the second cycle of ion beam figuring.

	Slope error rms (S.E) and best fit value of ellipse parameter θ								
	Lane 1			Lane 2			Lane 3		
	Specified ellipse	Best fit ellipse		Specified ellipse	Best fit ellipse		Specified ellipse	Best fit ellipse	
Instrument	S.E (nrad)	S.E (nrad)	θ (mrad)	S.E (nrad)	S.E (nrad)	θ (mrad)	S.E (nrad)	S.E (nrad)	θ (mrad)
Diamond-NOM	172	148	3.002 41	168	139	3.002 22	205	187	3.001 67
Diamond HDX	220	195	2.997 23	138	120	2.997 72	236	198	2.995 68
HZB-NOM	477	209	3.011 72	452	111	3.011 62	453	192	3.010 49

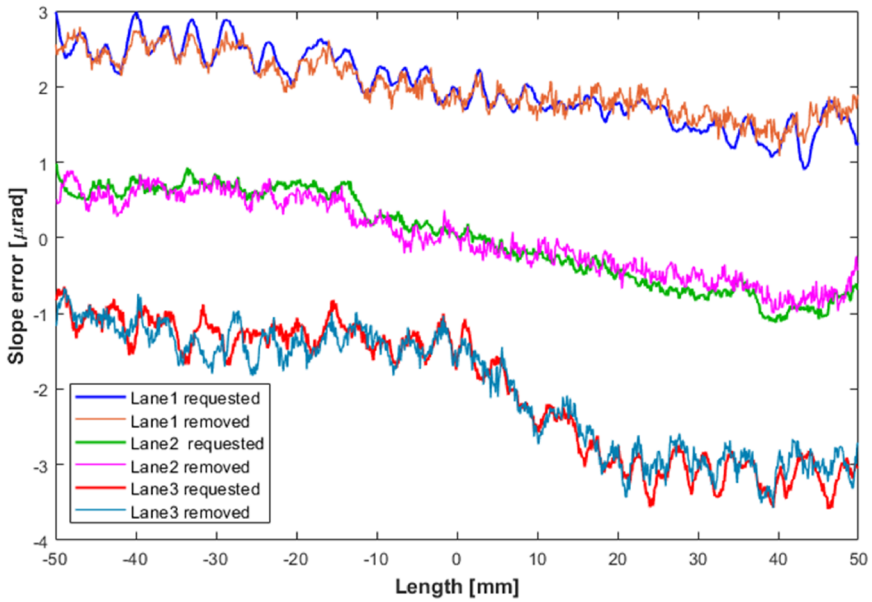

FIG. 11. For the second cycle of ion beam figuring, the requested slope error removal was in excellent agreement with the measured removal for each lane of the mirror, indicating accurate control of the deterministic polishing process at ZEISS. Curves are offset vertically for clarity.

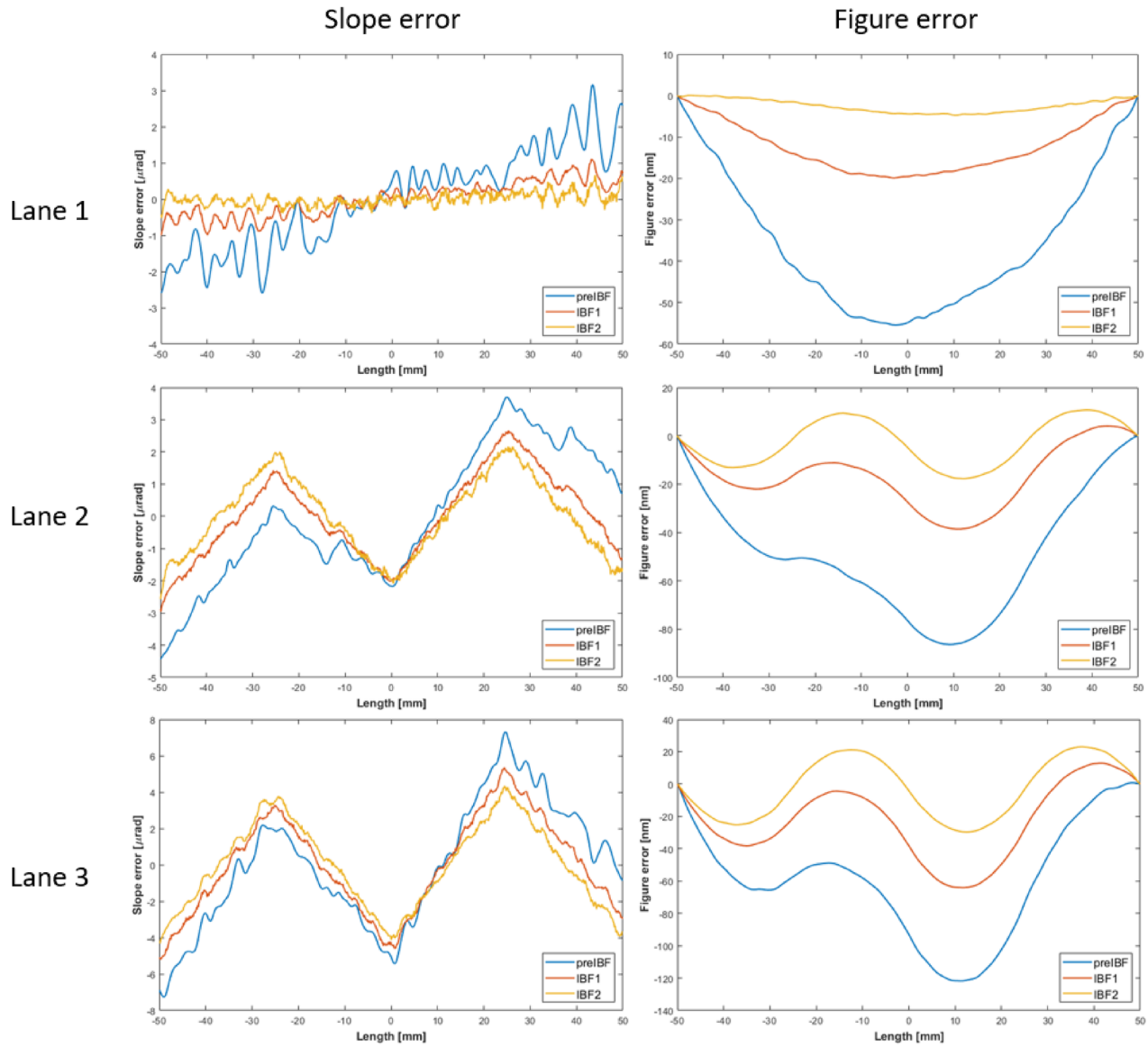

FIG. 12. All aspects of the mirror's quality were iteratively improved by two cycles of ion beam figuring for lane 1 (top row), lane 2 (middle row), and Lane 3 (bottom row). The three curves in each chart show the optical surface before (blue curves) and after the first (red curves) and second (orange curves) cycles of IBF correction. Slope error (left column) and figure error (right column), as measured by the Diamond-NOM, are relative to the specified ellipse.

TABLE VI. Summary of improvements to the x-ray mirror after each cycle of ion beam figuring.

	Improvements to the slope error (rms) (S.E) and height error (rms) (H.E) throughout the deterministic correction process relative to the specified ellipse					
	Lane 1		Lane 2		Lane 3	
Phase	S.E (nrad)	H.E (nm)	S.E (nrad)	H.E (nm)	S.E (nrad)	H.E (nm)
Before IBF	1323	16.6	1748	24.5	2190	29.2
After IBF1	471	6.2	615	8.8	875	12.2
After IBF2	172	1.6	168	1.8	205	1.6

lanes, and plots in the right column show the corresponding height errors. Note that the parabolic arcs in height correspond to triangular peaks in slope. Table VI provides a quantitative description of the improvements.

IV. CONCLUSIONS

This study reports on a rare opportunity for the cross-comparison of various types of optical metrology instruments used to characterize x-ray mirrors for XFEL and synchrotron light sources. Prior to the round-robin measurement exercise, a series of fiducial markers were added to the optic, enabling it to be aligned to within <100 μm relative to the coordinate system of each metrology device. This proved to be highly beneficial for locating surface topography features and precise extraction of 1D line profiles from 2D areal data. The fixed distance between selected pairs of fiducial features also helped cross-calibrate instrument magnification factors. For example, stretching the data to correct small, dimensional discrepancies in the zoom factor of Fizeau- or micro-interferometers to <0.1%.

For consistency, all datasets were analyzed using Diamond's standard ellipse-fitting algorithms. However, in the future, unprocessed datasets could be shared throughout the community to benchmark different analysis techniques, including Fourier filtering and ellipse fitting. The goal is a community-wide standardization and transparency of analysis. Ideally, all parties would use the same freely available, open-source software, such as PyLOSt stitching software,[52] developed as part of the MooNpics collaboration. This project also provided valuable lessons to guide standardization of various protocols, including safe packaging and logistics for transportation of fragile optics; improved documentation for inspection and test reports; and better use of metadata incorporation to record experimental conditions.

In many cases, excellent reproducibility was achieved between European optic manufacturers and partnership facilities when each lab independently and "blindly" measured the mirror. The three NOM slope profiling instruments, which each utilize the same model of autocollimator, differed by <0.01% in measuring the ellipse parameter θ for each lane of the mirror prior to IBF. A valuable outcome of the project was the identification of calibration and scaling issues with several instruments. These problems were subsequently corrected, thereby improving measurement reproducibility within the optical metrology community.

Guided by high-quality metrology data provided by the collaboration, two cycles of ion beam figuring were sequentially applied to the optic at ZEISS. This process improved all aspects of the mirror's quality, including correcting the ellipse parameters; reducing the absolute slope error (relative to the specified ellipse) from ~1500 to <200 nrad rms; and improving the shape of the parabolic arcs. It is hoped that future papers will provide corresponding details about the ultra-flat and spherical mirrors, which were also part of the MooNpics round-robin exercise. Ultimately, it is hoped that close cooperation with industrial partners and improved reproducibility of optical metrology will lead to further improvements in the production quality of x-ray optics to benefit XFEL and synchrotron light facilities around the world.

ACKNOWLEDGMENTS

The authors thank all MooNpics collaborators for openly sharing their metrology data and scientific expertise. We also thank the customs and logistics experts at each facility for their support to safely transport optics between facilities.

CALIPSOplus is an Integrating Activity for Advanced Communities in reply to the call INFRAIA-01-2016 (Material Sciences and Analytical facilities/Synchrotron radiation sources and Free Electron Lasers) in Horizon2020 the European Framework Program for Research and Innovation. This project has received funding from the European Union's Horizon 2020 Research and Innovation programme under Grant Agreement No 730872.

AUTHOR DECLARATIONS

Conflict of Interest

The authors have no conflicts to disclose.

Author Contributions

Simon G. Alcock: Formal analysis (equal); Investigation (equal); Methodology (equal); Project administration (equal); Supervision (equal); Writing – original draft (equal). **Ioana-Theodora Nistea**: Data curation (equal); Formal analysis (equal); Investigation (equal); Methodology (equal); Writing – review & editing (equal). **Murilo Bazan da Silva**: Data curation (equal); Formal analysis (equal); Investigation (equal); Methodology (equal); Writing – review & editing (equal). **Kawal Sawhney**: Supervision (equal). **Norman Niewrzella**: Investigation (equal); Resources (equal). **Holger Lasser**: Investigation (equal); Resources (equal). **Amparo Vivo**: Data curation (equal); Investigation (equal); Methodology (equal); Writing – review & editing (equal). **Ray Barrett**: Conceptualization (equal); Funding acquisition (equal); Project administration (equal); Supervision (equal); Writing – review & editing (equal). **Jana Buchheim**: Investigation (equal); Methodology (equal). **Grzegorz Gwalt**: Investigation (equal); Methodology (equal). **Frank Siewert**: Conceptualization (equal); Investigation (equal); Project administration (equal); Writing – review & editing (equal). **Sibylle Spielmann**: Investigation (equal); Methodology (equal). **Uwe Flechsig**: Data curation (equal); Investigation (equal); Methodology (equal). **Silja Schmidtchen**: Conceptualization (equal); Investigation (equal); Methodology (equal); Project administration (equal); Writing – review & editing (equal). **Maurizio Vannoni**: Conceptualization (equal); Investigation (equal); Methodology (equal); Project administration (equal). **Josep Nicolas**: Investigation (equal); Methodology (equal). **Muriel Thomasset**: Investigation (equal); Methodology (equal). **Francois Polack**: Investigation (equal); Methodology (equal).

DATA AVAILABILITY

The data that support the findings of this study are available from the corresponding author upon reasonable request.

REFERENCES

[1] J. P. Sutter, S. G. Alcock, I. T. Nistea, H. Wang, and K. Sawhney, "Active and adaptive X-ray optics at diamond light source," Synchrotron Radiat. News **35**, 8–13 (2022).

[2]D. Cocco, G. Cutler, M. Sanchez del Rio, L. Rebuffi, X. Shi, and K. Yamauchi, "Wavefront preserving X-ray optics for synchrotron and free electron laser photon beam transport systems," Phys. Rep. **974**, 1–40 (2022).
[3]S. Matsuyama, T. Inoue, J. Yamada, J. Kim, H. Yumoto, Y. Inubushi, T. Osaka, I. Inoue, T. Koyama, K. Tono, H. Ohashi, M. Yabashi, T. Ishikawa, and K. Yamauchi, "Nanofocusing of X-ray free-electron laser using wavefront-corrected multilayer focusing mirrors," Sci. Rep. **8**(1), 17440 (2018).
[4]A. Majhi, R. Shurvinton, P. C. Pradhan, M. Hand, W. Gu, M. B. Da Silva, S. Moriconi, I. Nistea, S. G. Alcock, H. Wang, and K. Sawhney, "Sub-nanometre quality X-ray mirrors created using ion beam figuring," J. Synchrotron Radiat. **31**, 706–715 (2024).
[5]D. L. Voronov, T. Wang, S. Park, L. Huang, E. M. Gullikson, F. Salmassi, C. Austin, H. A. Padmore, and M. Idir, "Nanometer flat blazed x-ray gratings using ion beam figure correction," Opt. Express **31**(21), 34789–34799 (2023).
[6]T. Wang, L. Huang, Y. Zhu, M. Vescovi, D. Khune, H. Kang, H. Choi, D. W. Kim, K. Tayabaly, N. Bouet, and M. Idir, "Development of a position–velocity–time-modulated two-dimensional ion beam figuring system for synchrotron x-ray mirror fabrication," Appl. Opt. **59**, 3306 (2020).
[7]T. Hänsel, A. Nickel, A. Schindler, and H.-J. Thomas, "Ion beam figuring surface finishing of x-ray and synchrotron beam line optics using stitching interferometry for the surface topology measurement," in *Frontiers in Optics 2004/Laser Science XXII/Diffractive Optics and Micro-Optics/Optical Fabrication and Testing* (Optical Society Group, 2004), paper OMD5.
[8]Z. Zhang, C. F. Cheung, J. Guo, and C. Wang, "Pressure-dependent material removal rate model of fluid jet polishing," Int. J. Mech. Sci. **281**, 109517 (2024).
[9]K. Yamauchi, H. Mimura, K. Inagaki, and Y. Mori, "Figuring with subnanometer-level accuracy by numerically controlled elastic emission machining," Rev. Sci. Instrum. **73**, 4028 (2002).
[10]S. Matsuyama, S. Yasuda, J. Yamada, H. Okada, Y. Kohmura, M. Yabashi, T. Ishikawa, and K. Yamauchi, "50-nm-resolution full-field X-ray microscope without chromatic aberration using total-reflection imaging mirrors," Sci. Rep. **7**(1), 46358 (2017).
[11]S. G. Alcock and S. Cockerton, "A preferential coating technique for fabricating large, high quality optics," Nucl. Instrum. Methods Phys. Res., Sect. A **616**, 110–114 (2010).
[12]P. Bras, S. Labouré, A. Vivo, F. Perrin, and C. Morawe, "Differential deposition applied to x-ray mirror substrates," Proc. SPIE **12576**, 1257607 (2023).
[13]G. E. Ice, J. S. Chung, J. Z. Tischler, A. Lunt, and L. Assoufid, "Elliptical x-ray microprobe mirrors by differential deposition," Rev. Sci. Instrum. **71**, 2635–2639 (2000).
[14]S. Liu, H. Wang, J. Hou, Q. Zhang, X. Chen, B. Zhong, and M. Zhang, "Combined processing strategy based on magnetorheological finishing for monocrystalline silicon x-ray mirrors," Appl. Opt. **61**(19), 5575–5584 (2022).
[15]R. E. Riveros, M. P. Biskach, K. D. Allgood, J. D. Kearney, M. Hlinka, A. Numata, and W. W. Zhang, "Fabrication of monocrystalline silicon x-ray mirrors," Proc. SPIE **11119**, 1111908 (2019).
[16]W. I. Kordonski and S. D. Jacobs, "Magnetorheological finishing," Int. J. Mod. Phys. B **10**, 2837–2848 (1996).
[17]See http://www.calipsoplus.eu/joint-research-activities-jra/jra1-moonpics/ for information about the aims and deliverables of the MooNpics project.
[18]S. G. Alcock, K. J. S. Sawhney, S. Scott, U. Pedersen, R. Walton, F. Siewert, T. Zeschke, F. Senf, T. Noll, and H. Lammert, "The Diamond-NOM: A non-contact profiler capable of characterizing optical figure error with sub-nanometre repeatability," Nucl. Instrum. Methods Phys. Res., Sect. A **616**, 224–228 (2010).
[19]I. Lacey, R. D. Geckler, A. Just, F. Siewert, T. Arnold, H. Paetzelt, B. V. Smith, and V. V. Yashchuk, "Optimization of the size and shape of the scanning aperture in autocollimator-based deflectometric profilometers," Rev. Sci. Instrum. **90**, 021717 (2019).
[20]R. D. Geckeler, A. Just, M. Krause, and V. V. Yashchuk, "Autocollimators for deflectometry: Current status and future progress," Nucl. Instrum. Methods Phys. Res., Sect. A **616**, 140–146 (2010).
[21]J. Nicolas, P. Pedreira, I. Šics, C. Ramírez, and J. Campos, "Nanometer accuracy with continuous scans at the ALBA-NOM," Proc. SPIE **9962**, 996203 (2016).
[22]F. Siewert, H. Lammert, and T. Zeschke, "The nanometer optical component measuring machine," in *Modern Developments in X-Ray and Neutron Optics*, edited by A. Erko, M. Idir, T. Krist, and A. G. Michette (Springer, Berlin, Heidelberg, 2008), pp. 193–200.
[23]I.-T. Nistea, S. G. Alcock, M. Bazan da Silva, and K. Sawhney, "Diamond-VeNOM: A high-speed slope profiler for characterizing x-ray mirrors," Proc. SPIE **12695**, 126950A (2023).
[24]L. Assoufid, N. Brown, D. Crews, J. Sullivan, M. Erdmann, J. Qian, P. Jemian, V. V. Yashchuk, P. Z. Takacs, N. A. Artemiev, D. J. Merthe, W. R. McKinney, F. Siewert, and T. Zeschke, "Development of a high-performance gantry system for a new generation of optical slope measuring profilers," Nucl. Instrum. Methods Phys. Res., Sect. A **710**, 31–36 (2013).
[25]L. Huang, J. Nicolas, and M. Idir, "Repeatability analysis of one-dimensional angular-measurement-based stitching interferometry," Opt. Express **26**, 20192 (2018).
[26]L. Huang, T. Wang, K. Tayabaly, D. Kuhne, W. Xu, W. Xu, M. Vescovi, and M. Idir, "Stitching interferometry for synchrotron mirror metrology at National Synchrotron Light Source II (NSLS-II)," Opt. Lasers Eng. **124**, 105795 (2020).
[27]L. Huang, T. Wang, J. Nicolas, A. Vivo, F. Polack, M. Thomasset, C. Zuo, K. Tayabaly, D. Wook Kim, and M. Idir, "Two-dimensional stitching interferometry for self-calibration of high-order additive systematic errors," Opt. Express **27**, 26940 (2019).
[28]P. J. de Groot, L. L. Deck, and T. Glaschke, "Characterizing the resolving power of laser Fizeau interferometers," Proc. SPIE **10829**, 1082905 (2018).
[29]V. V. Yashchuk, K. Munechika, S. Rochester, P. Z. Takacs, I. Lacey, and K. Yamada, "Performance of plane wavefront Fizeau interferometers in power spectral density measurements with tilted plane optics," Proc. SPIE **13150**, 1315006 (2024).
[30]M. B. da Silva, S. G. Alcock, I. T. Nistea, and K. Sawhney, "A Fizeau interferometry stitching system to characterize X-ray mirrors with sub-nanometre errors," Opt. Lasers Eng. **161**, 107192 (2023).
[31]A. Vivo, R. Barrett, and F. Perrin, "Stitching techniques for measuring X-ray synchrotron mirror topography," Rev. Sci. Instrum. **90**, 021710 (2019).
[32]A. Rommeveaux and R. Barrett, "Micro-stitching interferometry at the ESRF," Nucl. Instrum. Methods Phys. Res., Sect. A **616**, 183–187 (2010).
[33]Q. Wu, Q. Huang, W. Zhang, Z. Shi, M. Li, C. Zhang, Y. He, H. Luo, J. Yu, W. Gu, Z. Zhang, and Z. Wang, "Subaperture moving strategy and related systematic errors in stitching interferometry of X-ray mirrors," Opt. Express **32**(26), 45691–45706 (2024).
[34]H. Mimura, H. Yumoto, S. Matsuyama, K. Yamamura, Y. Sano, K. Ueno, K. Endo, Y. Mori, M. Yabashi, K. Tamasaku, Y. Nishino, T. Ishikawa, and K. Yamauchi, "Relative angle determinable stitching interferometry for hard x-ray reflective optics," Rev. Sci. Instrum. **76**, 045102 (2005).
[35]Y. Liu, M. Seaberg, D. Zhu, J. Krzywinski, F. Seiboth, C. Hardin, D. Cocco, A. Aquila, B. Nagler, H. J. Lee, S. Boutet, Y. Feng, Y. Ding, G. Marcus, and A. Sakdinawat, "High-accuracy wavefront sensing for x-ray free electron lasers," Optica **5**(8), 967–975 (2018).
[36]L. Hu, H. Wang, O. Fox, and K. Sawhney, "Fast wavefront sensing for X-ray optics with an alternating speckle tracking technique," Opt. Express **30**(18), 33259–33273 (2022).
[37]L. Rebuffi, X. Shi, Z. Qiao, M. J. Highland, M. G. Frith, A. Wojdyla, K. A. Goldberg, and L. Assoufid, "Real-time machine-learning-driven control system of a deformable mirror for achieving aberration-free X-ray wavefronts," Opt. Express **31**(13), 21264–21279 (2023).
[38]M. Idir, D. Cocco, and L. Huang, "Special issue 'EUV and X-ray wavefront sensing,'" Sensors **22**, 3940–3943 (2022).
[39]A. Rommeveaux, L. Assoufid, H. Ohashi, H. Mimura, K. Yamauchi, J. Qian, T. Ishikawa, C. Morawe, A. T. Macrander, A. Khounsary, and S. Goto, "Second metrology round-robin of APS, ESRF and SPring-8 laboratories of elliptical and spherical hard-x-ray mirrors," Proc. SPIE **6704**, 67040B (2007).
[40]A. Rommeveaux, M. Thomasset, D. Cocco, and F. Siewert, "The COST P7 round robin for slope measuring profilers," in *Modern Developments in X-Ray and Neutron Optics*, edited by A. Erko, M. Idir, T. Krist, and A. G. Michette (Springer, Berlin, Heidelberg, 2008), pp. 213–218.
[41]A. Rack, L. Assoufid, W. K. Lee, B. Shi, C. Liu, C. Morawe, R. Kluender, R. Conley, and N. Bouet, "Hard X-ray multilayer mirror round-robin on the wavefront preservation capabilities of W/B4C coatings," Radiat. Phys. Chem. **81**, 1696–1702 (2012).

[42]D. Laundy, K. Sawhney, I. Nistea, S. G. Alcock, I. Pape, J. Sutter, L. Alianelli, and G. Evans, "Development of a multi-lane X-ray mirror providing variable beam sizes," Rev. Sci. Instrum. **87**, 051802 (2016).
[43]C. Mao, H. Jiang, Y. He, D. Liang, X. Lan, S. Yan, D.-m. Shu, and A. Li, "Compensation for gravitational sag of bent mirror," Nucl. Instrum. Methods Phys. Res., Sect. A **853**, 20–26 (2017).
[44]S. Ferrer, M. Krisch, F. de Bergevin, and F. Zontone, "Evaluation of the anticlastic curvature of elastically bent crystals for X-ray focusing optics," Nucl. Instrum. Methods Phys. Res., Sect. A **311**, 444–447 (1992).
[45]R. Shurvinton, H. Wang, P. Pradhan, I.-T. Nistea, S. Alcock, M. Bazan Da Silva, A. Majhi, K. Sawhney, and K. Sawhney, "Ion beam figuring for X-ray mirrors: History, state-of-the-art and future prospects," J. Synchrotron Radiat. **31**, 655–669 (2024).
[46]J. P. Sutter, M. Amboage, S. Hayama, and S. Díaz-Moreno, "Geometrical and wave-optical effects on the performance of a bent-crystal dispersive X-ray spectrometer," Nucl. Instrum. Methods Phys. Res., Sect. A **621**, 627–636 (2010).
[47]P. J. de Groot, "The instrument transfer function for optical measurements of surface topography," J. Phys. Photonics **3**, 024004 (2021).
[48]E. Novak, C. Ai, and J. C. Wyant, "Transfer function characterization of laser Fizeau interferometer for high spatial frequency phase measurements," Proc. SPIE **3134**, 114–121 (1997).
[49]I. Lacey, K. Anderson, J. Dickert, R. Geckeler, A. Just, F. Siewert, B. V Smith, and V. V Yashchuk, "Transfer of autocollimator calibration for use with scanning gantry profilometers for accurate determination of surface slope and curvature of state-of-the-art x-ray mirrors," Proc. SPIE **11109**, 1110905 (2019).
[50]V. V. Yashchuk, S. Rochester, I. Lacey, and S. Babin, "Super-resolution surface slope metrology of x-ray mirrors," Rev. Sci. Instrum. **91**, 075113 (2020).
[51]F. Siewert, J. Buchheim, and T. Zeschke, "Characterization and calibration of 2nd generation slope measuring profiler," Nucl. Instrum. Methods Phys. Res., Sect. A **616**, 119–127 (2010).
[52]B. R. Adapa, *L'analyse de Front d'onde Appliquée à La Métrologie de Surface Optique* (Université Grenoble Alpes, 2020).